Research project

Czech Technical University in Prague

F4

Faculty of Nuclear Sciences and Physical Engineering
Department of Physics

Development of a new runaway electron diagnostics method based on strip semiconductor detectors

Bc. Marek Tunkl

Supervisor: Ing. Michal Marčišovský Ph.D.
September 2020

Acknowledgements

I would like to thank my supervisor Ing. Michal Marčišovský, Ph.D. for the valuable remarks and engagement through the writing of this research project.

Declaration

I hereby declare that I have written this thesis independently and on my own and only used the sources cited in bibliography.
I have no objection to usage of this work in compliance with the act §60 Law No. 121/2000 Coll. (Copyright Act), and with the rights associated with the copyright act including changes in the act.

Prague, September 2020

Abstract

Runaway electrons may emerge during discharge in a tokamak plasma. They can cause severe damage to plasma-facing components or adjacent diagnostics. In this research project, the mechanisms of RE formation and their interactions relevant for diagnostics are described. Furthermore, this work summarizes the properties of semiconductors and semiconductor detectors. Semiconductor strip detector with PH32 readout chip and LYSO scintillation detector with a silicon photomultiplier (SiPM) are described. And finally, the results of measurements with these detectors on tokamak GOLEM are presented.

Keywords: LYSO, PH32, runaway electrons, semiconductor detectors, SiPM, tokamak

Supervisor: Ing. Michal Marčišovský Ph.D.
Department of Physics,
Faculty of Nuclear Sciences and Physical Engineering,
Czech Technical University in Prague

Abstrakt

Během plazmatického výboje v tokamaku mohou vzniknout unikající elektrony (RE). Tyto elektrony způsobit vážné poškození povrch komory tokamaku nebo přilehlou diagnostiky. V tomto výzkumném úkolu jsou popsány mechanismy tvorby RE a jejich interakce relevantní pro diagnostiku. Dále tato práce shrnuje vlastnosti polovodičů a polovodičových detektorů. Je zde popsán stripový polovodičový detektor s vyčítacím čipem PH32 a scintilační detektor LYSO se silikonovým fotonásobičem (SiPM). Nakonec jsou prezentovány výsledky měření s těmito detektory na tokamaku GOLEM.

Klíčová slova: LYSO, PH32, polovodičové detektory, SiPM, tokamak, ubíhající elektrony,

Překlad názvu: Vývoj nové diagnostiky ubíhajících elektronů na bázi křemíkových stripových detektorů

Contents

Introduction

Demand for electricity rises with the growth of the human population and with technological progress. But the primary power source, fossil fuels, has to be reduced due to the emission of greenhouse gasses. So-called renewable resources are usually not stable since their production fluctuates, and current electricity storage methods are inefficient. Nuclear power plants are being rejected for safety reasons, but an alternative to fission power could be fusion.

Thermonuclear fusion is the source of energy in stars. Achieving fusion on Earth is possible as well, but it is definitely not easy. After 60 years of fusion research, a tokamak ITER is being built. This device should prove that it is possible to confine plasma in magnetic fields and heat it with enough efficiency, so the fusion produces more energy than consumes.

Plasma confinement faces problems with instabilities. In tokamaks, one of the most detrimental instabilities are disruptions - sudden loss of plasma confinement. During the disruption, runaway electrons (RE) may be generated. REs are one of the kinetic instabilities occurring in plasma. In small or medium tokamaks, they do not pose a severe threat, but they can pose a danger to the first wall and surrounding diagnostics in large devices. For a threat that RE poses for tokamak devices, there is undergoing investigation on their generation and mitigation.

Semiconductor detectors are widely used in high energy physics as particle detectors. They have good energetic, temporal, and space resolution. This work is focused on the development of semiconductor detectors for runaway electrons diagnostics. The first chapter introduces plasma physics and tokamaks. The second chapter discusses runaway electrons, mechanisms of their generation, their losses, and methods of diagnostics. The third describes the properties of semiconductor materials and semiconductor detectors. The fourth chapter is dedicated to diagnostics based on semiconductor detectors and their calibration. In the fifth chapter, results from measurements with these detectors are presented.

Chapter 1

Fusion and tokamaks

1.1 Thermonuclear fusion

Fusion is the nuclear reaction of light nuclei, during which energy is released. The fusion of two protons, as occurs in the Sun, is not feasible in laboratory conditions. The best candidate is a reaction of deuterium and tritium:

$$ {}^{2}_{1}\mathrm{D} + {}^{3}_{1}\mathrm{T} \rightarrow {}^{4}_{1}\mathrm{He}\ (3.5\,\mathrm{MeV}) + {}^{1}_{0}\mathrm{n}\ (14.1\,\mathrm{MeV}). \tag{1.1} $$

From the dependence of cross-section on the temperature (fig. 1.1) can be seen, that temperature necessary for fusion is in order of keVs. With that temperature, DT gas will inevitably become ionized; it will be in the state of plasma.

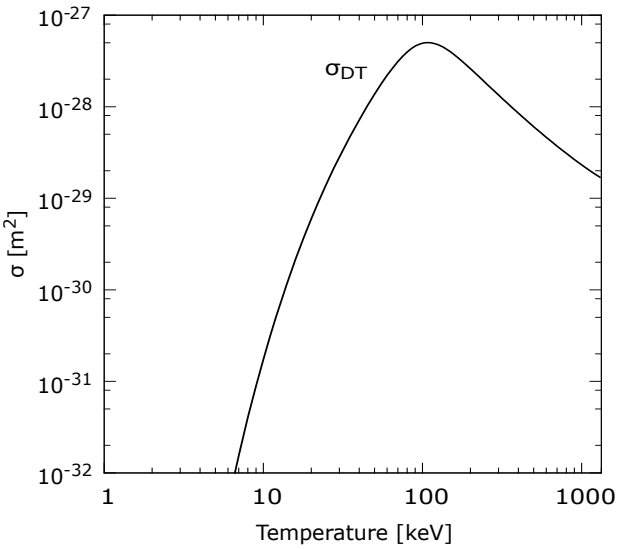

Figure 1.1: The cross-section of the DT reaction [1].

Fusion power plant must produce more energy then it is needed for plasma

heating and confinement. Such condition is determined by the Lawson criterion

$$n_{\mathrm{p}}\tau_{\mathrm{E}} \geq \frac{12k_{\mathrm{B}}T}{\langle\sigma\nu\rangle\ E_{\mathrm{f}}}, \tag{1.2}$$

where n_{p} is the plasma density, τ_{E} energy confinement time, k_{B} the Boltzmann constant, $\langle\sigma\nu\rangle$ reactivity, and E_{f} the energy of charged products of fusion contributing to plasma heating. For DT fusion is right-hand side function of temperature with a minimum at $T = 30\,\mathrm{keV}$. Hence $n_{\mathrm{p}}\tau_{\mathrm{E}} \geq 1.5 \cdot 10^{20}\,(m^{-3}s)$ [1].

Such condition can be fulfilled with high plasma density ($n_{\mathrm{p}} \approx 10^{29}\,\mathrm{m}^3$) and short confinement time ($\tau_{\mathrm{E}} \approx 10^{-9}\,\mathrm{s}$). This approach is used in inertial fusion when laser drivers compress small fuel pellet. With sufficient compression, pellet heats up, and fusion reaction will burn trough pellet. Following micro-explosion will heat the reactor wall.

The opposite approach is magnetic confinement. The low plasma density ($n_{\mathrm{p}} \approx 10^{20}\,\mathrm{m}^3$) is compensated by a long confinement time ($\tau_{\mathrm{E}} \approx 1\,\mathrm{s}$). Currently, most developed devices for magnetic confinement are tokamaks and stellarators. Both devices uses a helical magnetic field for plasma confinement.

1.2 Plasma

Plasma is a quasi-neutral ionized gas consisting of charged and neutral particles that behave collectively. In quasi-neutral gas, a macroscopic volume seems neutral, even though it contains many charged particles. In plasma, the electric potential of inserted charged particle is shielded at 1/e of its original value in the distance of Debye length

$$\lambda_{\mathrm{D}} = \sqrt{\frac{\varepsilon_0 k_{\mathrm{B}}}{\sum_\alpha Q_\alpha^2 n_\alpha / T_\alpha}}, \tag{1.3}$$

where ε_0 is the vacuum permittivity, k_{B} the Boltzmann constant a Q_α, n_α, T_α are charge, density, and temperature of α-type plasma particles.

The Coulomb interaction between charged particles has a longer range than the binary collision. Because of this, we talk about the collective behavior of the plasma.

A charged particle loses one degree of freedom in the magnetic field B. Electrons and ions undergo Larmor rotation with the radius R_{R} and angular frequency ω_{c} given by

$$\omega_{\mathrm{c}} = \frac{qB}{m}, \qquad R_{\mathrm{L}} = \frac{mv_\perp}{qB}, \tag{1.4}$$

where q is particle charge, m its mass and $v_\perp$ velocity component perpendicular to the magnetic field [2].

1.3 Tokamak

Tokamak (an abbreviation of the russian "toroidalnaja kamera i magnitnitnie katushki") is a toroidal device for the plasma confinement using magnetic fields. In a tokamak, two main magnetic fields are used to confine plasma inside the vacuum vessel. The toroidal field coils produce the toroidal magnetic field B_ϕ, and the poloidal magnetic field B_θ is created by the plasma current and outer poloidal field coils (fig. 1.2). The combination of these fields results in the helical magnetic field, which holds the plasma inside the chamber. Current inside the plasma is driven by a central solenoid, so plasma acts as the secondary winding of a transformer. The poloidal field generated by Ampere's law is usually in the order of magnitude lower than the toroidal field. This results in low helicity, so when charged particle performs one poloidal cycle, it travels multiple turns in toroidal direction. The number of cycles in the toroidal direction divided by the poloidal ones is denoted as the safety factor q. If q is an irrational number, the trajectory of the particle never crosses itself, and creates a coherent surface. Plasma is stable for $q > 1$, and tokamaks usually operate with $q \approx 3$ on the plasma boundary.

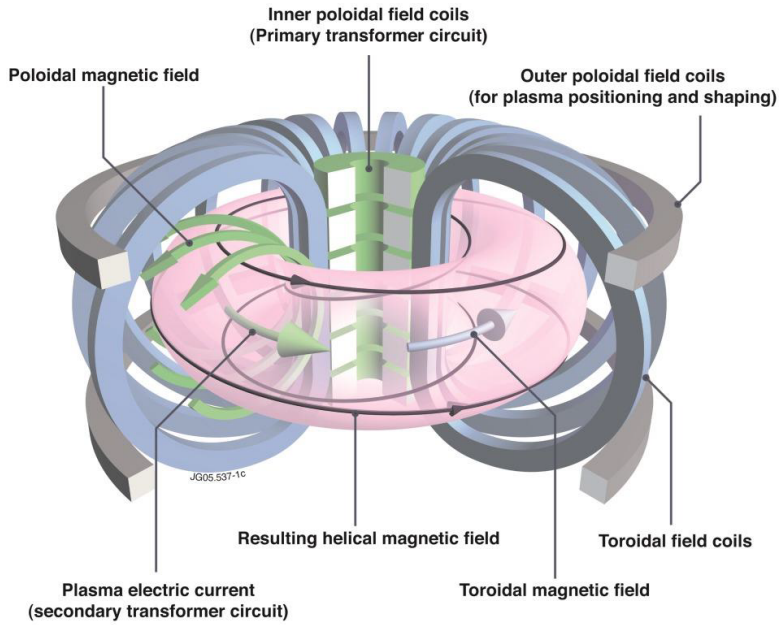

Figure 1.2: Schematic of tokamak coils and magnetic fields [3].

Plasma tends to expand and drift this configuration, so in addition to the coils mentioned above, a set of poloidal coils are used to help shape the plasma. Older tokamaks operate with circular plasma, but modern devices form plasma to D shape. This is beneficial because there is a stronger magnetic field on the inner side of the vacuum vessel since its intensity decreases as $1/R$ for distance from central solenoid R. Therefore, the middle of the torus is called the high filed side (HFS), and the outer part of the torus is referred to as the low field side (LFS).

Magnetic field lines form the surface of constant magnetic flux. These surfaces are not always closed inside the tokamak vessel. If the particle diffuses to the trajectory on this flux surface, it will inevitably crash into the tokamak first wall. The last closed flux surface (LCFS) is defined as the edge of the confined plasma. The region where flux surfaces are no longer closed inside the tokamak is called a scrape-of-layer (SOL). For better separation of plasma and first wall, the divertor configuration may be used. Instead of obstacle limiting plasma radius – limiter, the magnetic configuration is altered to contain X-point – the point where $B_\theta = 0$. With divertor configuration, plasma interacts with a region in SOL, but LCFS is not in contact with any solid material. Configuration with limiter and with divertor are illustrated in figure 1.3 [1].

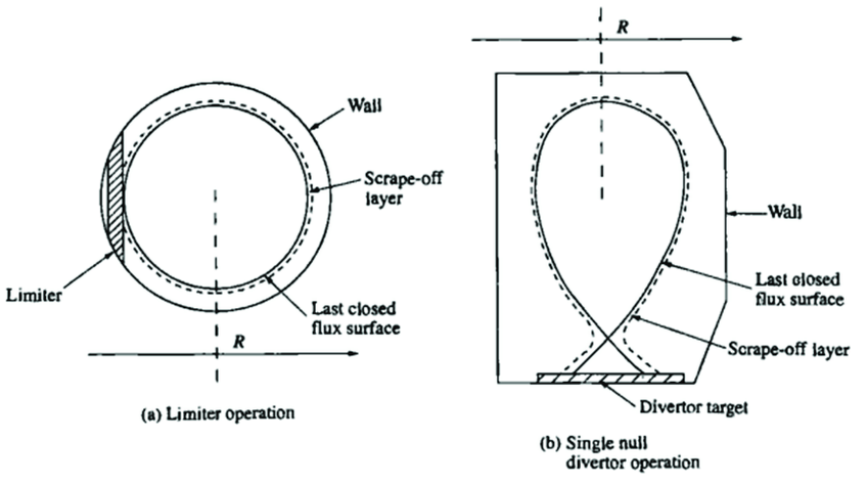

Figure 1.3: Schematics of limited plasma (left) and configuration with divertor (right) [1].

1.3.1 GOLEM

GOLEM is a small tokamak located in the Faculty of Nuclear Sciences and Physical Engineering. It was constructed in the USSR under the name TM-1. Since 1977 it has served at the Institute of Plasma Physics as CASTOR (Czechoslovak Academy of Sciences TORus). In 2007 moved to FNPSE, where it is used for education and probe testing. The parameters of GOLEM tokamak are in table 1.1.

Major radius	$R_0 = 0.4\,\mathrm{m}$
Minor radius	$r_0 = 0.1\,\mathrm{m}$
Limiter radius	$a = 0.085\,\mathrm{m}$
Toroidal magnetic field	$B_\mathrm{t} < 0.8\,\mathrm{T}$
Plasma current	$I_\mathrm{pl} < 8\,\mathrm{kA}$
Discharge length	$\tau \approx 15\,\mathrm{ms}$
Plasma density	$n_\mathrm{e} \approx 10^{18}\,\mathrm{m}^{-3}$

Table 1.1: The principal parameters of GOLEM tokamak [4].

Chapter 2

Runaway electrons

2.1 Generation of runaway electrons

In tokamaks, runaway electrons may emerge from several processes that are divided into two groups - the primary and the secondary. The first group covers mechanisms, which do not need the previous existence of suprathermal electrons. These are Dreicer's mechanism, which occurs when the electric field is strong, the fast particles are not slowed down collisionally and therefore, acceleration prevails. And hot tail mechanism during which the rapid cooling of the bulk plasma makes the fast tail of the Maxwellian distribution almost collisionless and thus creates a runaway electron population. Except for these processes, there other sources that can also generate the runaway seed. Among these are the tritium decay, cosmic radiation, Compton scattering, magnetic reconnection, etc. The secondary mechanism contributes to the exponential growth of runaway population.

2.1.1 Dreicer's mechanism

This mechanism carries the name of H. Dreicer, who described the behavior of runaway electrons in hydrogen plasma [5]. His description is non-relativistic; the influence of relativistic effects will be discussed later. Dreicer's description is a solution of the Fokker-Planck equation

$$\frac{\partial f_\alpha}{\partial t} + (\mathbf{v}_\alpha \cdot \boldsymbol{\nabla}_\mathrm{x}) f_\alpha + \left(\frac{\mathbf{F}_\alpha}{m_\alpha} \cdot \boldsymbol{\nabla}_\mathrm{v}\right) f_\alpha = S_{\alpha\beta} \tag{2.1}$$

for electron beam described by Dirac distribution function with interaction with plasma with the Maxwellian distribution.

$$f_\alpha = n_\alpha \delta(\mathbf{v}_\alpha - v(t)) \ , \quad f_\beta = n_\beta \left(\frac{m_\beta}{2\pi k_\mathrm{B} T_\beta}\right)^{3/2} \mathrm{e}^{-\frac{m_\beta v_\beta^2}{2k_\mathrm{B}T_\beta}} . \tag{2.2}$$

The first moment of the Fokker-Planck equation can be solved analytically with the result

$$m_\mathrm{e} \frac{\partial v}{\partial t} = eE - eE_\mathrm{D} \psi\left(\frac{v}{v_\mathrm{te}}\right) \ , \tag{2.3}$$

where E_D is Dreicer field, ψ Chandrasekhar's function, and v_{te} temperature of the bulk plasma.

$$E_{\mathrm{D}} = \frac{n_{\mathrm{e}} e^3 \ln \Lambda}{4\pi\epsilon_0^2 k_{\mathrm{B}} T_{\mathrm{e}}}\ , \qquad \psi(x) = \frac{4}{\sqrt{\pi}x^2}\int_0^x \xi^2 \mathrm{e}^{-\xi^2}\mathrm{d}\xi\ . \tag{2.4}$$

Dreicer field depends on plasma density n_{e} and electron temperature T_{e}, $\ln\Lambda$ is Coulomb logarithm, which can be assumed to be constant for tokamak plasma.

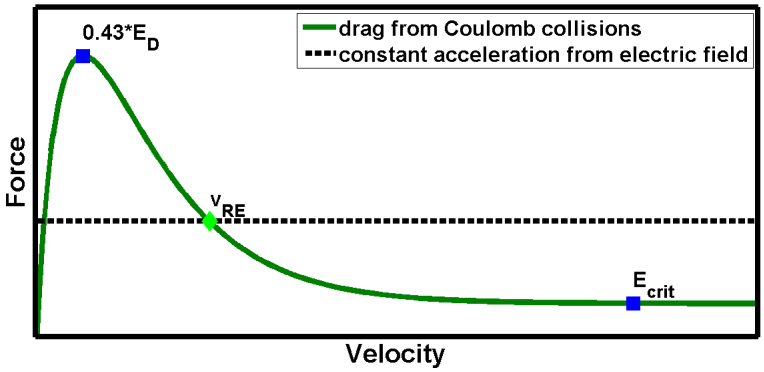

Figure 2.1: Dependence of friction force on particle velocity [6].

The last term in equation (2.3) represents friction force slowing down the electron. As shown in figure 2.1, friction force has a maximum at thermal velocities v_{te}. When external electric field E exceeds Drecier field E_{D}, all electrons run away. Even though E is small, some electrons are in the runaway region. Chandrasekhar's function behaves as x^{-2} for large values. Thus friction force is proportional to v^{-2} for large velocities. Using high velocity limit we can derive from (2.3) that equilibrium occurs for critical velocity v_{c}.

$$v_{\mathrm{c}} = \sqrt{\frac{n_{\mathrm{e}} e^4 \ln\Lambda}{4\pi\varepsilon^2 m_{\mathrm{e}} E}}, \tag{2.5}$$

An electron moving along an electric field with a velocity greater than v_{c} will run away. Critical velocity can be used for estimation of the number of possible RE in plasma with a Maxwell distribution [7]

$$n_{\mathrm{RE}} = \int_{v_{\mathrm{c}}}^{\infty} n_{\mathrm{e}} \left(\frac{m_{\mathrm{e}}}{2\pi k_{\mathrm{B}} T_{\mathrm{e}}}\right)^{3/2} \mathrm{e}^{-\frac{m_{\mathrm{e}} v^2}{2k_{\mathrm{B}} T_{\mathrm{e}}}} \mathrm{d}v. \tag{2.6}$$

This estimate is nonrelativistic and does not take into account changes to electron distribution function.

Relativistic effects modify friction force acting on electrons and introduce a local minimum, which corresponds to a critical electric field or Connor-Hastie field [8]

$$E_{\mathrm{CD}} = \frac{n_{\mathrm{e}} e^3 \ln\Lambda}{4\pi\varepsilon^2 m_{\mathrm{e}} c^2}. \tag{2.7}$$

which acts as a threshold for runaway electrons. Because Coulomb logarithm is almost constant for tokamak plasma, the CD field is a function of density $E_{\mathrm{CD}} \cong n_{\mathrm{e}} \cdot 0.8 \cdot 10^{-20}$. Furthermore, in tokamak particles flow curved magnetic field lines and produce synchrotron radiation, so the critical field's effective value is estimated to be about five times larger than E_{CD} [9].

Kruskal and Berrnstein derived growth of runaway electron population by primary mechanism as

$$\left(\frac{\mathrm{d}n_{\mathrm{RE}}}{\mathrm{d}t}\right)_{\mathrm{Dreicer}} = C\frac{n_{\mathrm{e}}^2 e^4 \ln\Lambda}{4\pi\varepsilon_0^2 m_{\mathrm{e}}^2 v_{\mathrm{te}}^3}\left(\frac{E}{E_{\mathrm{D}}}\right)^{-\frac{3}{16}(1+Z_{\mathrm{eff}})} \exp\left(-\frac{E_{\mathrm{D}}}{4E} - \sqrt{\frac{(1+Z_{\mathrm{eff}})E_{\mathrm{D}}}{E}}\right), \tag{2.8}$$

where C constant in order of unity, Z_{eff} effective charge $Z_{\mathrm{eff}} = \sum_i \frac{n_i Z_i}{n_{\mathrm{e}}}$ [8].

The Dreicer's mechanism serves as the seed of RE, and these electrons are multiplied further by the secondary mechanism. This mechanism is significant in small and medium-sized tokamaks with lower plasma densities. In larger tokamaks, RE seed could be generated via a hot tail mechanism or other sources.

2.1.2 Hot tail mechanism

The hot-tail mechanism is linked to instabilities in plasma, mainly to plasma disruptions. Disruption may be caused by numerous events, often by the presence of impurities. The first part of plasma disruption is thermal quench; it is followed by the current quench due to loss of conductivity. If the cooling is swift, cooling time is comparable to electrons' collision time, and then the fast electrons do not have time to thermalize as the rest of bulk plasma. These fast electrons form a hot-tail of the distribution function. In the cooling plasma, the critical velocity decreases, and the hot-tail electrons can become runaway electrons. Formation of the hot tail from Maxwellian distribution is illustrated in figure 2.2. The growth rate of the runaway electron population by a hot tail mechanism can be estimated by formula

$$\left(\frac{\mathrm{d}n_{\mathrm{RE}}}{\mathrm{d}t}\right)_{\mathrm{hot-tail}} = 4\pi\frac{\mathrm{d}}{\mathrm{d}t}\int_{v_{\mathrm{c}}}^{\infty}(v^2 - v_{\mathrm{c}}^2) f \mathrm{d}v\ , \tag{2.9}$$

where v_{c} is the critical velocity for the runaway generation and f Maxwellian distribution function [10].

2.1.3 Secondary mechanism

A close collision between a runaway and a thermal electron can give enough energy for the thermal electron to jump into the runaway region while the primary electron remains runaway. These so-called knock-on collisions are quite rare in tokamak plasma, but in a large tokamak, the avalanche mechanism plays the central role in the runaway electron generation. The secondary mechanism is also called "avalanche" because it can result in an exponential growth of the runaway density. This is much faster than

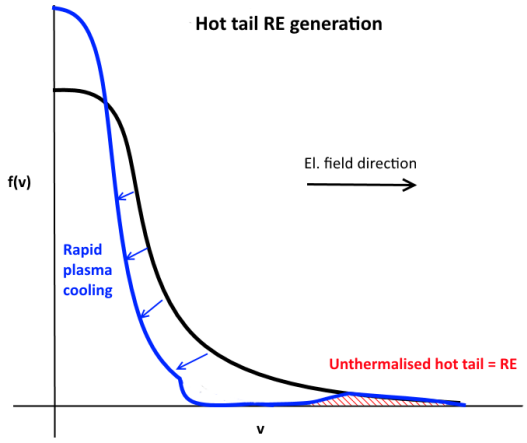

Figure 2.2: Formation of the hot tail mechanism from Maxwellian distribution during the thermal quench [7].

the linear growth in the case of pure Dreicer mechanism. This process is secondary because it requires a seed of REs in the plasma. The growth of the population of RE due secondary mechanism can be approximated with formula by Rosenbluth and Putvinski

$$\left(\frac{\mathrm{d}n_{\mathrm{RE}}}{\mathrm{d}t}\right)_{\mathrm{avalanche}} = \frac{I_{\mathrm{pl}}}{I_{\mathrm{A}} \ln \Lambda} , \tag{2.10}$$

where I_{pl} is plasma current, $I_{\mathrm{A}} = 4\pi\varepsilon_0 m_0 c^3/e \approx 17.1\,\mathrm{kA}$ is the Alfvén current and the Coulomb logarithm $\ln \Lambda$ [11]. In tokamaks with large current (such as ITER), this can be a very powerful process and a small number of REs can be multiplied. According to predictions, the RE current in ITER can reach up to 10 MA [12].

2.2 Runaway losses

2.2.1 Particle loss

For particle loss, a simple diffusion approximation can be used

$$\left(\frac{\mathrm{d}n_{\mathrm{RE}}}{\mathrm{d}t}\right)_{\mathrm{loss}} = \frac{1}{r}\frac{\partial}{\partial r}\left(D_{\mathrm{RR}}\frac{\partial n_{\mathrm{RE}}}{\partial r}\right) , \; D_{\mathrm{RR}} = \pi q v_{\parallel} R \left(\frac{\delta B}{B}\right)^2 \tag{2.11}$$

with D_{RR} as a diffusion coefficient. q is the safety factor, $v_{\parallel} \simeq c$ is the parallel velocity, R is the major radius and $\delta B/B$ is the normalized magnetic perturbation amplitude. This diffusion model known to overestimate [13].

2.2.2 Radiation loses

Besides particle loss from the plasma, REs can lose energy through radiation caused due to their acceleration.

Bremsstrahlung

The bremsstrahlung denotes the radiation process, which occurs during Coulomb collisions, and that is caused by the abrupt acceleration of the incident particles. Electron radiates with power

$$P_{\text{brems}} = \frac{4}{137} n_{\text{e}} (Z_{\text{eff}} + 1) m_{\text{e}} c^3 \beta\gamma r_{\text{e}}^2 (\ln 2\gamma - \frac{1}{3}) \ , \tag{2.12}$$

where m_{e} and n_{e} are electron mass and density, Z_{eff} effective charge, $r_{\text{e}} = e^2/(4\pi\varepsilon_0 \text{e} c^2)$ is classical electron radius and γ and β are Lorentz factor, electron velocity normalised to speed of light respectively [14].

Synchrotron radiation

The typical radiation of electron with MeV energies is the synchrotron radiation. The RE gyrates around the magnetic field line in tokamak and emits synchrotron radiation. The power loss coming from the synchrotron radiation is expressed as

$$P_{\text{synch}} = \frac{2 r_{\text{e}} m_{\text{e}} c^3 \beta^4 \gamma^4}{3 R_{\text{c}}^2} \ , \tag{2.13}$$

where R_{L} is an electron Larmor radius trajectory [15].

2.3 Interaction of runaway electrons with matter

Electrons loses energy through collisions S_{c} and radiation S_{r}. During collisions, surrounding material is ionized. The energy loss per unit of length can be described by the Bethe formula

$$-\left(\frac{\text{d}E}{\text{d}x}\right)_{\text{c}} = \frac{2\pi e^4 N Z}{m_{\text{e}} v^2} \left(\ln \frac{m_{\text{e}} v^2 E}{2 I^2 (1-\beta^2)} - (\ln 2) \left(2\sqrt{1-\beta^2-1+\beta^2} \right) \right.$$
$$\left. + (1-\beta^2) + \frac{1}{8} \left(1 - \sqrt{1-\beta^2} \right) \right), \tag{2.14}$$

where N and Z are the density of particles ie. atomic number, I ionisation potential, m_{e} a e electron mass and charge and β fraction of electron velocity v and speed of light c [16].

When electron momentum changes it bremsstrahlung occurs. Loss from radiation are described by

$$-\left(\frac{\text{d}E}{\text{d}x}\right)_{\text{r}} = \frac{NEZ(Z+1)e^4}{137 m_{\text{e}}^2 c^4} \left(4 \ln \frac{2E}{m_{\text{e}}} - \frac{4}{3} \right). \tag{2.15}$$

Because of dependence on E and Z^2 the Bremsstrahlung is significant only for high energies and for absorber material of large atomic number. Bremsstrahlung to collision loss radio is $\frac{S_{\text{r}}}{S_{\text{c}}} \approx \frac{EZ}{700}$ for energy in MEVs [16]. Total energy loss is $S = -\left(\frac{\text{d}E}{\text{d}x}\right)_{\text{r}} - \left(\frac{\text{d}E}{\text{d}x}\right)_{\text{c}}$.

2.3.1 Interaction with the first wall

Energetic electron hitting the limiter or tokamak wall produces bremsstrahlung in the X-ray region. In dependency of the electron's energy, another electron from the material can be excited, or if with large enough energy, the electron may excite nuclei, which produces γ radiation. Nevertheless, all electrons are absorbed in a vacuum vessel. X-ray radiation produced by electrons may be absorbed and reemitted multiple times.

2.3.2 Interaction of X-ray radiation

Almost all energy of RE is transferred to photons during interaction of RE with plasma particles or with the first wall of the tokamak. These energetic photons may interact with matter in different ways depending on their energy and the material. Measurement of X-ray radiation is a basic diagnostic for runaway electrons. Main channels of photon interaction are photoelectric absorption, Compton scattering, and pair production. Dependence on the incident photon's energy and the interacting atoms of the material is shown in figure

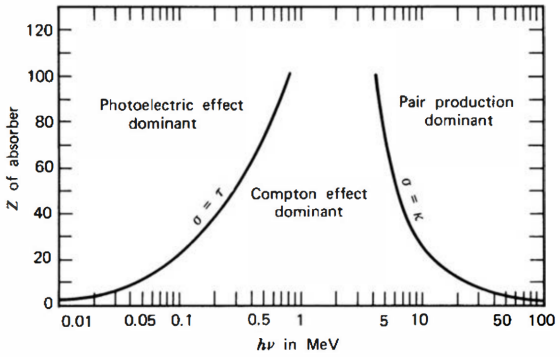

Figure 2.3: Mechanisms of the photon interaction with matter depending on the Z number of the target atoms and the photon's energy [16].

Photoelectric absorption

Photon is absorbed in one of the electrons in the inner shell of the atom. If its energy is larger than the binding energy E_b of absorber electron, the electron is ejected with energy

$$E = h\nu - E_\mathrm{b}, \tag{2.16}$$

where h is Planck constant and ν frequency of the photon. After undergoing this process, the liberated electron may interact with other electrons in the material. The vacancy created by ionization in the atom's inner shell is filled with an electron from the higher shell. This results in releasing either characteristic radiation or an Auger electron.

Compton scattering

Compared to the photoelectric absorption, the incoming photon is scattered on either a free electron or one in an atom's outer shell. A recoil electron and incident photon are scattered with angle θ (fig. 2.4). From the conservation of energy and momentum, we can calculate the energy of scattered photon as

$$h\nu' = \frac{h\nu}{1 + \frac{h\nu}{m_e c^2}(1 - \cos\theta)}, \tag{2.17}$$

where $h\nu$ is the energy of the photon prior to the scattering, $m_e c^2$ is rest-mass of an election.

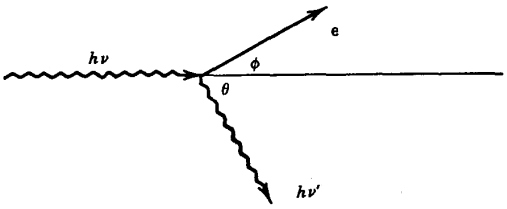

Figure 2.4: A diagram Compton of the scattering [16].

Pair production

When photon energy exceeds double the mass of an election ($h\nu > 1.022\,\mathrm{MeV}$), an pair production may occur. The incoming photon converts into an electron-positron pair within the Coulomb field of a nucleus. The emerging pair carries excess energy. The positron annihilates shortly, producing energetic photon [16].

2.3.3 Photo-neutrons

If high energetic photons interacts with the nuclei, it may produce neutron trough reaction (γ,n). For this process threshold energy of the photon is required to overcome the binding energy of the nucleus. For neutron emission of carbon this threshold energy is about 10 MeV [16], [17].

2.4 Runaway Electron Diagnostics

RE diagnostic methods rely mostly on radiation, they can be divided into two groups. The first measures radiation of the relativistic electron impact into the tokamak first wall. The second group focuses on the radiation of the movement charged particle, and they can measure properties of the REs confined inside a tokamak. In addition, some information can be delivered from magnetic diagnostics.

2.4.1 Soft X-Ray diagnostics

REs in the plasma produce bremsstrahlung by collisions with the ions of the plasma's impurities, and this radiation is usually in the SXR region. Due to the low frequency of collisions of passing electrons, the produced braking radiation is weak and difficult to detect. Another source of bremsstrahlung in the SXR spectrum could occur if the lost REs hit the tokamak wall.

2.4.2 Hard X-Ray diagnostics

When RE hits the first wall with the energy higher than a few tens of keV, the produced bremsstrahlung is usually in the HXR spectra. Scintillators are usually used for HXR detection and characterization of the RE loss. HXR detectors are usually placed outside the tokamak, but more localized measurements with detectors looking inside the vacuum vessel are also made [18].

2.4.3 Synchrotron radiation diagnostics

Synchrotron radiation occurs when charged relativistic particle changes its moment. In a tokamak, this is caused by the toroidal magnetic field. The radiation is emitted in the direction parallel to particle velocity. REs emit IR or even visible synchrotron radiation, and it can be observed with a camera in a counter-current tangential view.

2.4.4 Electron cyclotron emission diagnostics

This method uses the same radiative principle as the synchrotron radiation, but the electron cyclotron emission appears due to the Larmour rotation around the magnetic field line. Radiometers are used for ECE measurements. ECE is typically in the microwave region.

2.4.5 Cherenkov probes

The Cherenkov radiation occurs when a charged particle moves through a media with a higher velocity than the speed of light in that media. Cherenkov probe is placed near SOL acts as a localized detector for RE. The probe consists of a sensitive layer (e.g. aluminum nitride) inside a light-protected measuring head [19].

2.4.6 Magnetic diagnostics

Magnetic diagnostics are fundamental diagnostic methods in the tokamaks. Even though it is not used for RE observation, this diagnostics may provide some additional information on RE. The RE population acts as independent conductive media, so it influences the magnetic diagnostics. Toroidal electric

field E_{tor} plays an important role in the estimation of RE population, and it can also be used to estimate the maximum possible RE energy as

$$W_{\mathrm{max}} = ec \int_0^t E_{\mathrm{tor}} \mathrm{d}t, \tag{2.18}$$

where c is the speed of light and e electron charge.

Chapter 3

Semiconductor detectors

Semiconductor detectors are a type of solid-state detectors for ionizing radiation. Radiation passing through the detector creates a pair of electron and hole, which may be separated by an electric field. Then electron and hole drift to opposite sides of the sensor, and an induced signal is measured. Properties of semiconductor material and PN junction are used to reduce thermal noise. Usually, semiconductor detectors are packed to the matrix of pixels or sensitive strips.

3.1 Band structure of a semiconductor

To understand the principle of semiconductors, we must know how the band structure in solids looks like. Energetic states of an electron bounded to an atom are discrete. In the crystal structure of N atoms, their interaction changes the distribution of energetic states. States which should be degenerated splits to bands of allowed energies, as shown in picture 3.1.

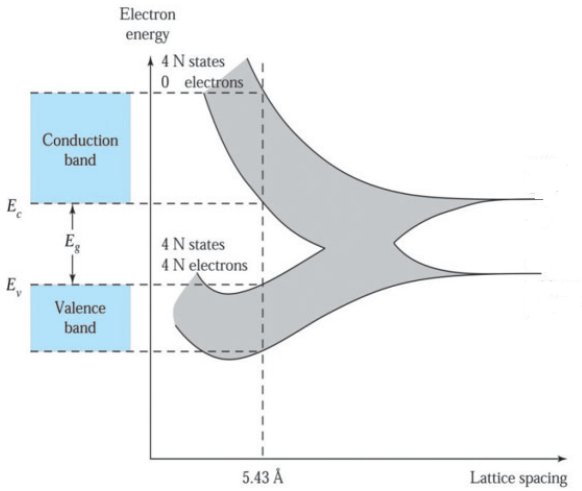

Figure 3.1: Allowed energies for electron in crystalline lattice in silicon [20].

The distribution of allowed bands determines if the material is conductor, semiconductor, or insulator. The valence band is the highest ground

state band, electrons in this band are responsible for chemical bonds. The conduction band usually has higher energy, and electrons in it can move freely. The gap between valence and conduction band E_g determines how the material behaves. In insulators, band gap is too wide for electrons to overcome. Whereas in conductors bands are either close to each other, they even overlap. Hence conductors have a large number of free electric carriers. Semiconductor lies in the middle of those cases [20], [21].

3.2 Properties of semiconductors

When an electron accepts energy at least equal to the energy difference corresponding to the band gap, it transfers to the conduction band, leaving a vacancy – a hole in the valence band. Thus, an electron-hole pair is created. In the presence of an outer electric field, an electron will move in one direction. The hole may be filled with an electron from other electron-hole pairs, which can be described as the hole movement. Electron and hole velocities are given by

$$\nu_e = -\mu_e E, \tag{3.1}$$
$$\nu_h = \mu_h E, \tag{3.2}$$

where μ_e and μ_h are mobilities of electrons and holes respectively, and E is the electric field. The mobility of holes is approximately 3× lower than the mobility of electrons. The increase of velocity is finite and is limited by the saturation velocity [16].

The electron-hole pair can be generated thermally or radiatively. The probability for the generation of an electron-hole pair depending on the temperature T is

$$p(T) = CT^{3/2} e^{-\frac{E}{2k_B T}}, \tag{3.3}$$

where C is a constant dependent on the semiconductor material, E_g is the band gap energy and k_B is the Boltzmann constant. Generated pair recombines shortly after creation, unless it is separated by the electric field.

3.2.1 Intrinsic and extrinsic semiconductors

Pure semiconductors are called intrinsic semiconductors. The number of holes and free electrons in this material is equal. The electron-hole pair can be generated only thermally or due to ionizing radiation. Properties of semiconductors are strongly affected by impurities present. These impurities may be added deliberately trough a process called doping. Doped semiconductors can have either more holes in the valence band or more free electrons in the conduction band than intrinsic materials.

- An n-type semiconductor is doped with impurities which act as electron donors. For tetravalent silicon, this can be achieved by adding pentavalent materials, e.g. phosphorus or arsenic. Atoms of dopant substitute silicon

in crystalline lattice and the excessive electrons are loosely bounded, creating an additional energy gap close to the conduction band. In n-type semiconductor electron dominates, this makes electrons the majority carrier.

- A p-type semiconductor is doped with acceptor impurities. Boron acts as an acceptor for silicon semiconductors. Its atoms have fewer electrons. Thus, a hole is created in place of an unsaturated covalent bond. An electron which fills the hole in this bond is attached slightly less than in typical bond, since one of the atoms in only trivalent. This creates a new energy band slightly higher to the valence band. In this case, holes are the majority carriers, while electrons are the minority carriers.

Band structure of n-type, p-type and intrinsic semiconductor is shown in figure 3.2

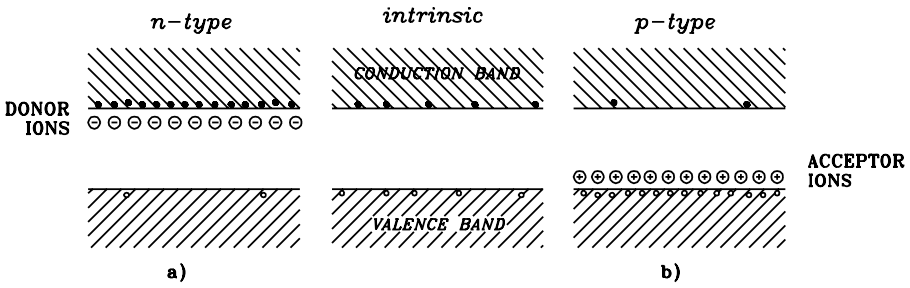

Figure 3.2: Band structure of : a) n-type semiconductor b) p-type semiconductor and intrinsic semiconductor in the middle [21].

3.3 PN junction

The PN junction is created on the boundary between p-type and n-type semiconductors in monocrystal. This junction is formed with alternative doping when half of the material is donor-doped, and the other half is acceptor-doped. Due to the diffusion of charge carriers and their recombination, a negative charge is created in p region and positive charge in n region of the junction. The induced electric field counteracts further diffusion. This creates a depletion region with no free charge carriers. The electron-hole pair created in depletion region is separated, and the electron is pushed to the n-side and holes to the p-side of the junction. This generates a measurable signal, which can be used for detecting ionizing radiation.

The depletion region is small, but its width can be increased through reverse biasing. When the external electric field is applied, with the positive voltage on the n-type side and negative voltage on the p-side of semiconductor, the resulting potential contributes to contact potential already present in the

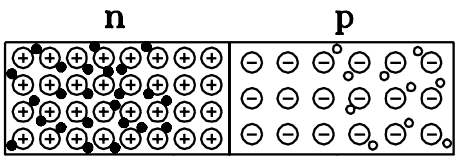

Figure 3.3: The PN junction. Depletion region without free electric carriers is created on both sides of the junction [21].

junction. The width of the depletion region d can be calculated from

$$d \simeq \sqrt{\frac{2\varepsilon V_{\mathrm{b}}}{eN}}, \tag{3.4}$$

where e is the electron charge, ε semiconductor permittivity and N concentration of dopant with lower concentration level at the junction. If the depletion region extends the whole volume, the diode is fully depleted.

Since there is a voltage across the junction, the depletion region behaves like a capacitor. The capacitance decreases with increasing reverse bias. For the capacitance applies

$$C = \frac{\varepsilon S}{d} \simeq S\sqrt{\frac{e\varepsilon N}{2V_{\mathrm{b}}}}. \tag{3.5}$$

In order to achieve the best resolution of the detector, a capacitance should be as low as possible. Therefore, the largest possible bias voltage is applied until full depletion is achieved. However, reverse bias can not be increased indefinitely, since large bias causes breakdown [16].

3.4 Semiconductor detectors

Depending on the type of radiation, electron-hole pairs are formed in the diode. This formation may take place directly or may involve the interaction of secondary particles produced by the primary radiation. Semiconductor sensors can be used for detection of

- visible or UV light – photon generates a single electron-hole pair.
- X-ray – since energy for pair creation is 3.6 eV, a many electron-hole pairs are created in small region. Photons interact via pair production, Compton scattering and electron pair production, as is discussed in 2.3.2.
- α particles – penetration depth of α particles is a few micrometers. As ionization (2.14) grows when velocity decreases, most pairs is created in the stopping point of the particle.
- β radiation – β particles have lower mass and ionizes less than α. Thus β particles penetrate to deeply into semiconductor volume and with high energy, they can even pass through it.

- High-energy charged particles – relativistic particles passes through the detector volume, producing uniform number of electron-hole pairs along its path.
- Nonrelativistic charged particles – particle deposits its energy in detector volume.

Depending on the type and energy of the particles, the doping profile and the size of the diode are used. Detection of neutrons and high energy photons is also possible, but the probability of interaction is too small, so semiconductor detectors alone are inappropriate for neutron and high-energy photon detection. Nevertheless other materials can be used to convert this radiation to forms more suitable for semiconductor detectors [21].

3.5 Strip detector with PH32 readout

The PH32 is a readout chip for strip detectors of ionizing radiation. It was developed by the Center of Applied Physics and Advanced Detection Systems (CAPADS) at FNSPE, CTU. The detector consists of a sensor and PH32 readout chip, an application-specific integrated circuit (ASIC), which converts an analog signal from sensor to a digital form. The detector can operate in two modes for energy range, low-gain allow measurement from 37 keV to 5 MeV (α particles) and high-gain mode from 7 keV to 40 keV (soft X-ray and β particles). Configuration of detector and readout of digital data is performed by SURE (SimpleUSB Readout Equipment), which acts as an interface between the chip and computer. Sensor consists of 32 strips, each 250 μm $\times$ 18 mm. Strips are n^+-on-p sensor of 525 μm thickness. The full depletion of the sensor occurs at -100 V bias [22].

3.5.1 ASIC

The PH32 chip is manufactured in 180 nm CMOS technology, channels of chip and sensor are wire bonded. Chip and bonding are covered in epoxy for protection. The chip consists of analog and digital part.

Analog part

Each channel of ASIC is connected to a sensor strip through AC coupling. A signal is amplified by the charge sensitive amplifier (CSA) and compared with the predefined threshold of the discriminator. The output from the discriminator is processed by the digital part of the chip. The CSA sensitivity can be adjusted by changing the feedback capacitance. Each channel contains multiple digital to analog converters (DAC), which allows us to adjust the current feedback of CSA (FDAC) and tune the threshold for discriminator (TDAC). Thus it is possible to calibrate each channel separately to obtain the equal output of CSA for all channels.

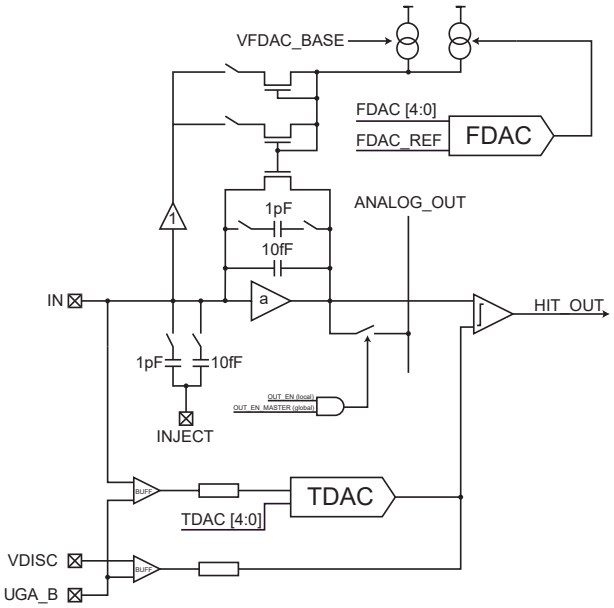

Figure 3.4: The diagram of the analog part of the ASIC detector PH32 [22].

Digital part

Pulses from the comparator are processed in the digital part of the chip. Input is processed when the digital shutter is open. Channel can be configured to four different modes of signal processing

- Hit count – counts how many times the threshold has been exceeded during the acquisition time.
- Deposited energy – using the internal clock, time over the threshold is measured. The height and duration of the pulse are proportional to deposited energy.
- Energy of first hit – similarly to the previous mode, the energy of the first detected particle is measured.
- Time of arrival – time between particle detection and the end of the shutter measured. This can be used to compute the time of flight of detected particle [23].

The output from the sensor, discriminator, and illustration of modes function is shown in figure 3.5. Measurements are stored in 16 bit asynchronous counter with overflow control. After acquisitions, data can be read by SURE. The time for readout and reset of the counter yields the detector's dead time, it is approximately 75 µs.

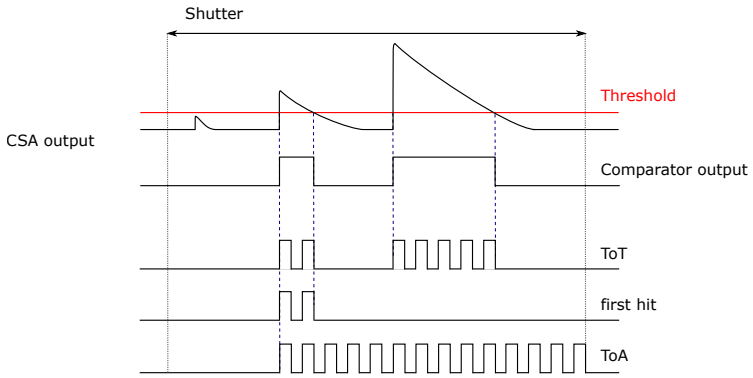

Figure 3.5: Principle of time over threshold (ToT) method in signal processing of PH32 chip.

3.6 Scintillation detectors

Scintillation material produces light when excited by ionizing radiation. A scintillator coupled with a photomultiplier, photodiode, or silicon photomultiplier, forms a detector. Many materials exhibit scintillation property, but most used are inorganic crystals or organic materials. These material types differ in principle responsible for light emission. Therefore organic and inorganic scintillators have different characteristics. The scintillator is characterized by light yield, a light pulse's decay time, energetic resolution, and spectrum of produced light. Properties of some scintillation materials are in table 3.1.

material	light yield [photons/MeV]	τ [ns]	λ_{max} [nm]	n [-]	ρ [g·cm^{-3}]
NaI(Tl)	38000	230	415	1.85	3.67
LSO	25000	47	420	1.82	7.4
LYSO	27600	45	420	1.81	7.1
YAP	18000	27	370	1.95	5.37
$LaBr_3$:Ce	63000	20	380	1.9	5.08

Table 3.1: Properties of selected scintillation materials [16]. τ – decay time, λ_{max} wavelength of maximum emission, n – reflective index, ρ – density [16], [24], [25]

3.6.1 Inorganic scintillators

Inorganic scintillators are typically crystals. In comparison to organic scintillators, they have a higher light yield, but longer decay time. Since inorganic scintillators have a high atomic number and density, they are used for γ ray spectroscopy.

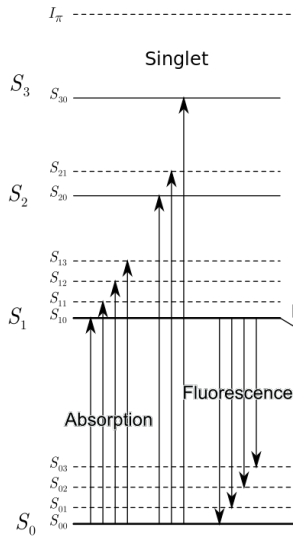

Figure 3.6: The band structure in organic scintillators. Incident photon excites an electron to higher energy states. After scintillator deexcites trough internal conversion to state S_{10}. The scintillation photon is released trough the transition to the ground vibration state [16].

In inorganic materials, the scintillation mechanism depends on the structure of the electron band structure. Scintillation crystals are insulators; their valence conduction band gap is about 20 eV (band gap is described in section 3.1 in more detail). Absorption of energy excites an electron to the conduction band. In a pure crystal, the electron returns releasing photon, but this process is not efficient. By dopping crystal with impurities (activators), introduces a new energy state in the forbidden gap. Through this new state, an electron can deexcite, releasing a photon of visible light.

3.6.2 Organic scintillators

Organic scintillators are plastics, liquids, or rarely crystals. Organic scintillators have a typically shorter decay time, but smaller light yield, which is non-linear for large energy doses.

The scintillation mechanism in organic materials arises from transitions in the energy levels of a single molecule. Such energy levels are shown in figure 3.6. Energy from a particle can be absorbed by exciting an electron to one of many excited states. A singlet (spin 0) states are labeled as S_i. Each of these states is subdivided to vibrational states (labeled as S_{ij}). Higher states S_2, S_3 deexcites quickly trough radiationless internal conversion. Vibration states also lose their energy. After a negligibly short time, the molecule is in S_{10} state. Scintillation light is released trough transition from S_{10} state to any ground vibrational state. Sometimes scintillation light has a too short wavelength. Hence another compound is added as "wave-shifter". This compound absorbs primary scintillation light and reemits it in a longer wavelength.

3.6.3 Photon measurement

Photomultiplier

The Photomultiplier tube is constructed as a vacuum tube containing a photocathode, several dynodes, and an anode. The photocathode converts incident light photons into low-energy electrons. The pulse of photoelectrons produced has a similar time duration to pulse from a scintillation crystal. The number of photoelectrons is too small for direct measurement [16].

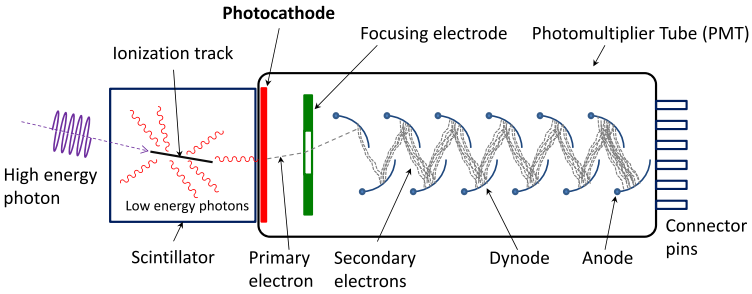

Figure 3.7: A schematic of a scintillator detector consisting of scintillation crystal and photomultiplier. A high energy photon is converted to visible light in the scintillator. A visible photon is converted to electron via the photoelectric effect and consequently amplified by series dynodes in a photomultiplier [26].

Photodiode

The operation principles of photodiode are very similar to the silicon particle detector described in section BB. A photodiode contains layers with different dopping, which form a PIN diode. A thin layer of highly doped p silicon (called p^+ layer) is followed by a slightly doped n-Si (called i) layer and ends with a highly doped n^+-Si layer. A transparent SiO_2 film present on top of the p+ layer. Applying a reverse bias creates an electric field in the depletion region, which separates electron-hole pairs created by incident photons. The photodiode gain is proportional to the number of incident photons, but due to the thermal creation of electron-hole pairs, a significant noise is present. This makes normal photodiode inconvenient for reading out scintillator low-intensity light. Avalanche photodiode (APD) has a particular doping profile that provides a high electric field in a specific area. This electric field provides sufficient energy for a charge carrier to trigger the ionization cascade. Avalanche photodiodes have higher gain than standard photodiodes. When a reverse bias is large enough, the silicon breaks down and becomes conductive. Therefore, a single electron-hole pair can be amplified into the macroscopic current. This is an analog to process in the Geiger-Müller tube. A special type of avalanche diode operating in Geiger mode is referred to as a single-photon avalanche diode (SPAD) [27].

Silicon photomultiplier

The single photon avalanche diode can not detect more than one photon, it is a digital detector. Once a photon hits SPAD, current flows through the diode and it has to be stopped. This can be done passively through the use of a resistor in series with SPAD. The resistor limits the current flowing through diode during breakdown, this lowers the voltage seen by the diode and halts the avalanche. Silicon photomultiplier (SiPM) is a device consisting of an array of SPAD all connected in parallel (see figure 3.8). SPAD with quenching resistor forms one microcell in SiPM.

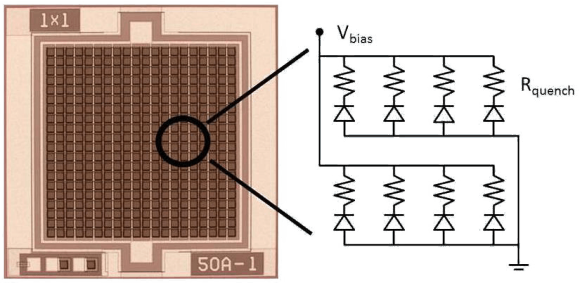

Figure 3.8: Silicon photomultiplier and connection scheme of SPADs and quenching resistors [28].

Dark count. A thermal electron can trigger an avalanche in SPAD, this creates a single photon signal in SiPM. The dark count is measured in pulse rate or pulse rate per area, since it increases linearly with area. The amount of noise-pulses increases with temperature and bias voltage.

Optical crosstalk. The optical cross talk occurs when the breakdown of one cell in a SiPM triggers an avalanche in a neighboring cell. During the breakdown in diode, photons can be emitted. These photons can travel to the neighboring cell directly, they can be reflected from window material on top of the sensor. Emitted photon can be absorbed by the same pixel, so the possibility of crosstalk decreases with microcell size.

Afterpulses. Impurities in silicon lattice can trap electric carrier. If the carrier is released after diode recovery, another pulse is triggered.

Chapter 4

Semiconductor based runaway electron diagnostics

4.1 The LYSO scintillation detector

Scintillation detector consists of $3 \times 3 \times 5\,\mathrm{mm}^3$ LYSO crystal and small SiPM.

LYSO. Lutetium-yttrium oxyorthosilicate ($Lu_{1.8}Y_{0.2}SiO_5$:Ce), also known as LYSO, is an inorganic scintillation crystal. For its high density and shorts decay time, LYSO crystals are often used in positron emission tomography (PET) and calorimetry in high-energy physics. Natural lutetium contains 2.6 % of ^{176}Lu which is a beta emitter with half life $3.78 \cdot 10^{10}$ y. Decay results in an excited state of ^{176}Hf and subsequent 3 gamma ray cascade of 307, 202, and 88 keV. The ctivity of Lu in the crystal is 184 Bq/cm3 [24].

SiPM. PM3315-WB-B0 SiPM manufactured by Ketek was used. This silicon photomultiplier consists of 38800 microcells each with size 15 µm. It has dark count rate between 0.5 MHz and 1.1 MHz, crosstalk probability between 7 %-20 %. Active area of size $3 \times 3\,\mathrm{mm}^2$ is covered in glass with refraction index 1.52 [29].

In order to increase the light collection efficiency, LYSO crystal was wrapped with white Teflon (PTFE) tape and optically coupled with SiPM by oil with refraction index 1.51.

4.1.1 Calibration

The calibration of the LYSO scintillation detector in energy was done with isotopes ^{214}Am, ^{133}Ba and ^{152}Eu with bias voltage 29.4 V. Measured spectra are in figures 4.1a – 4.1c. Calibration curve is in figure 4.1d

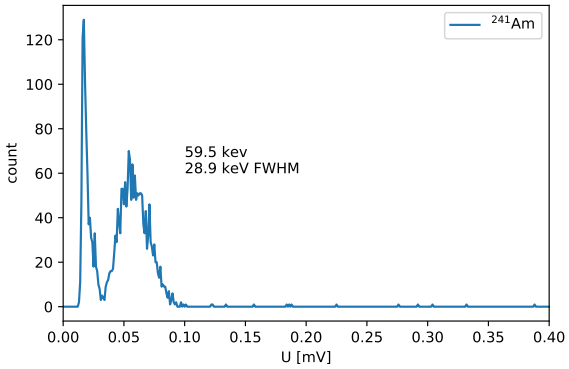

(a) : ^{214}Am

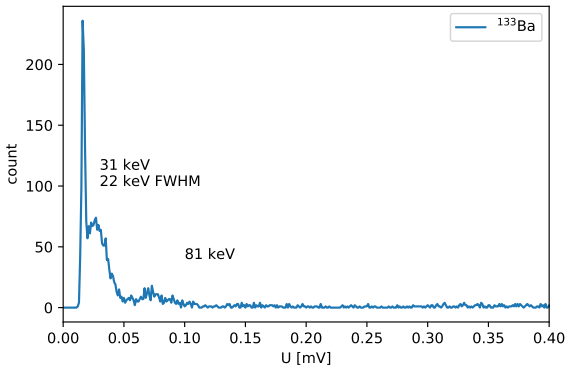

(b) : ^{133}Ba

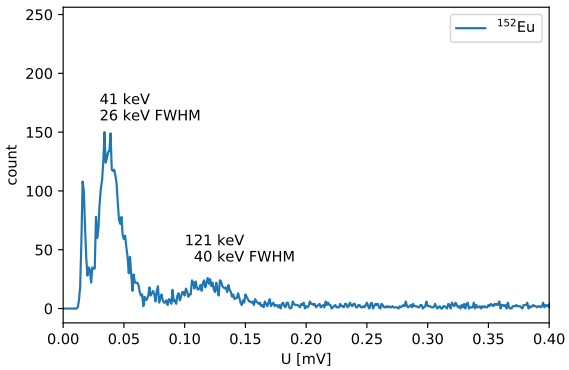

(c) : ^{152}Eu

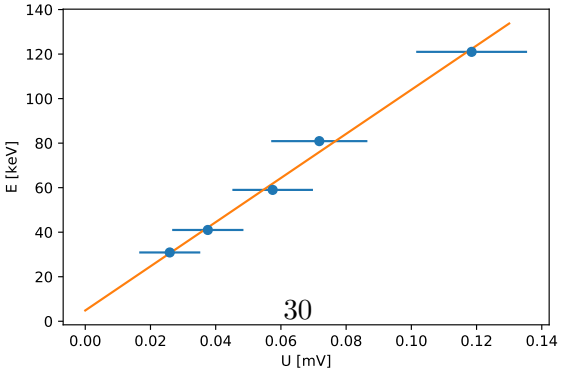

(d) : Calibration curve

Figure 4.1: Spectra of ^{214}Am, ^{133}Ba and ^{152}Eu and resulting calibration curve of output peak amplitude U vs. photon energy E for LYSO with SiPM.

4.2 The silicone strip detector

For this research project a newer version of the strip detector was used. In comparison to the detector used in the bachelor thesis it has shorter dead time it is mounted on a smaller PCB, but it has no analog output. Even though the detector was smaller (fig. 4.2) it has it had to be cut, so the sensor can be placed in the SOL region of the tokamak.

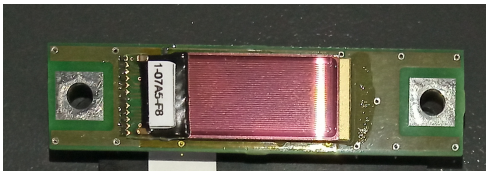

Figure 4.2: Photo of silicon strip detector.

The detector was inserted in metal box, which acts as electromagnetic shielding. The window for the sensor was covered with 3 µm thick aluminium foil, which prevents light from hitting the sensor. This setup was mounted on radial manipulator and placed inside the vacuum vessel of GOLEM tokamak. Detector is shown in figure 4.3.

Acquisition time was set to 150 µs, with a delay 90 µs. Total deposited energy in one frame was measured via ToT method.

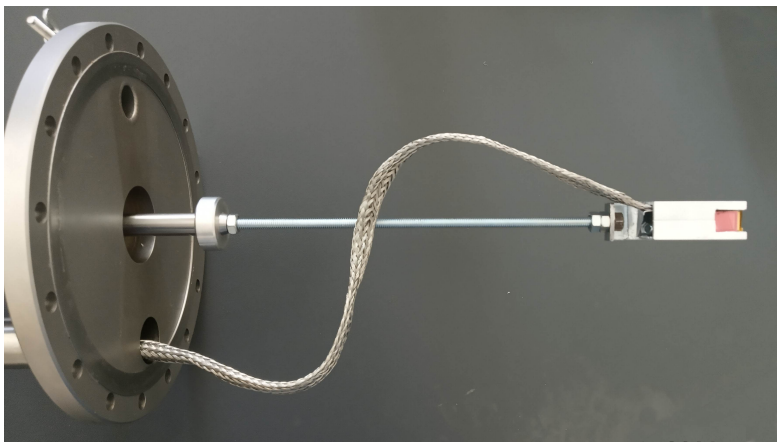

Figure 4.3: Strip detector on radial manipulator.

4.2.1 Calibration

Prior to inserting the detector into the tokamak, channels of the readout chip were equalized and sensor was calibrated in energy with ^{241}Am, the result is shown in figure 4.4.

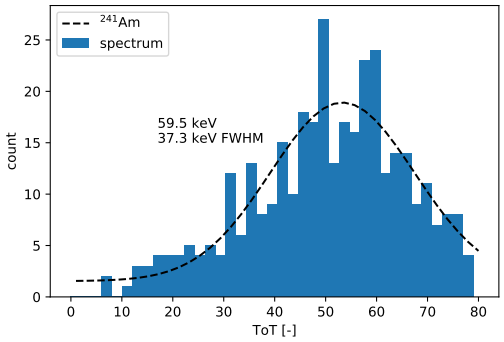

Figure 4.4: The spectrum of ^{214}Am, measured by strip detector.

4.3 Experiment setup

The layout of the diagnostics is shown in figure 4.5. The strip detector was inserted in small south port and the LYSO scintillation detector was placed next to the north-west port. From standard GOLEM diagnostics, the signal from NaI(Tl) and YAP scintillation detectors was measured and basic magnetic diagnostics was used.

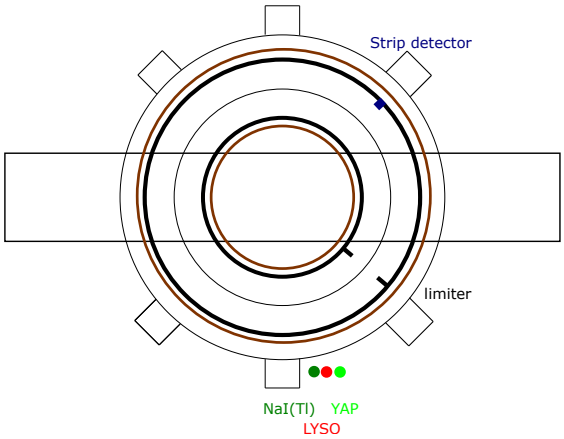

Figure 4.5: Layout of the diagnostics. Strip detector in small S port and scintillation detectors facing limiter.

Chapter 5

Results

5.1 LYSO

Shots with a moderate number of RE shows that LYSO with SiPM can be used for HXR diagnostics of RE. And unlike the detector with NaI(Tl), it has better capabilities to provide a spectrum detected radiation from a whole discharge because peaks in output do not add up, as is shown in figure 5.1. Obtained spectrum of detected radiation is shown in figure 5.1a and shows that maximum energy of RE was about 120 keV in discharge 33816.

But with the stronger HXR radiation. The pulse from individual detection is short but is followed by followed longer undershoot (fig. 5.3). This leads to the fall of the baseline for the next pulse. Consequently, the output signal is unusable; see figure 5.4. The pulse undershooting may result from inadequate impedance matching.

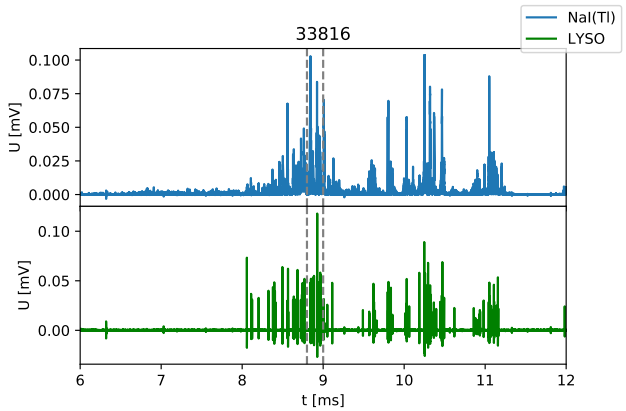

(a) : whole discharge

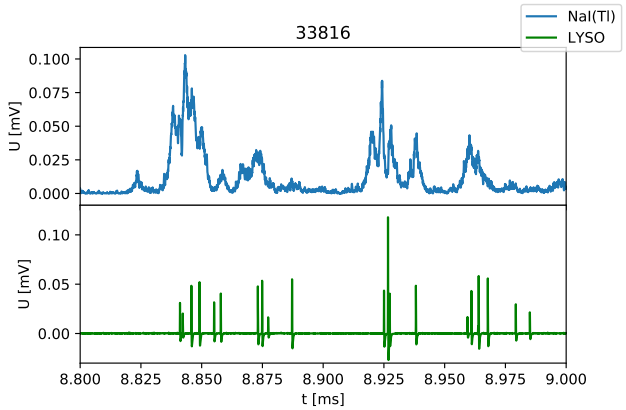

(b) : detail – peaks in NaI(Tl) add up, they are separated in LYSO

Figure 5.1: Output of NaI(Tl) with PMT and LYSO with SiPM for shot n. 33816

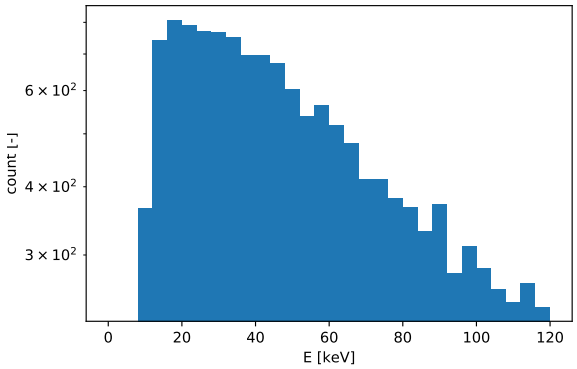

Figure 5.2: Spectrum of HXR obtained from LYSO scintillation detector in shot n. 33816

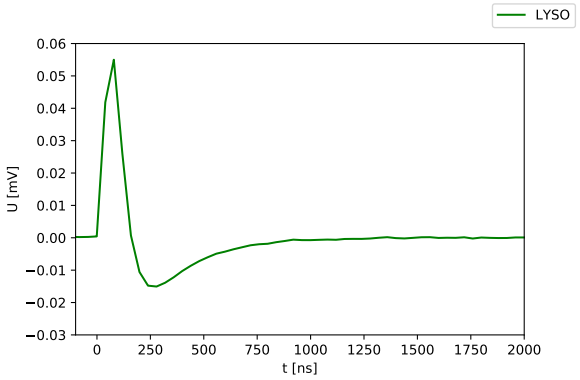

Figure 5.3: Single peak from SiPM. Narrow peak followed by long undershoot.

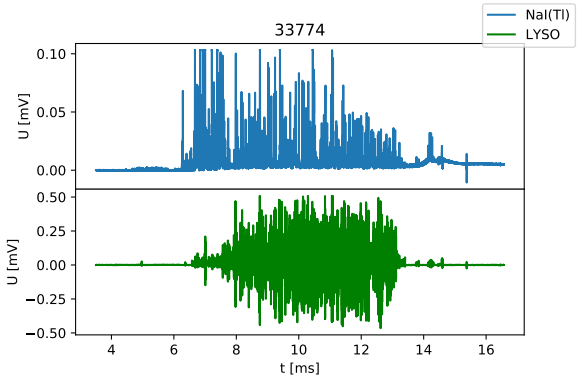

Figure 5.4: Shot n. 33816. Peaks adds up in NaI(Tl) and produce useful signal, but output from SiPM is distorted.

5.2 Silicon strip detector

The measurement from the strip matched the signal from scintillators. In one frame (150 µs), the deposited energy reached up to 15 MeV, as is shown in figures 5.5.

Dependence of total deposited energy on detector angular position is shown on figures 5.6a,5.6a. Both measurement was conducted with sensor in SOL, first figure corresponds to distance from plasma edge $d = 12$ mm, second to $d = 6$ mm. Note that this dependence is not strong, which suggests that electrons recoiling from limiter are also detected.

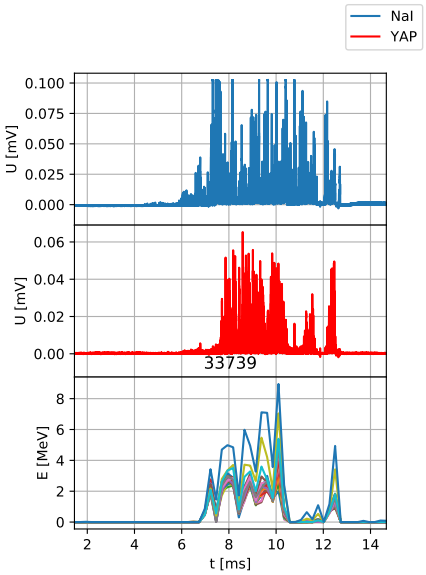

(a) : Shot n. 33739.
Strip detector 12 mm from plasma edge, oriented upwards.

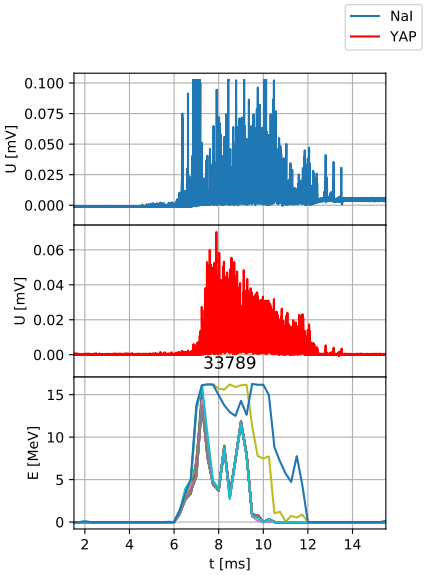

(b) : Shot n. 33739.
Strip detector 6 mm from plasma edge, oriented upwards.

Figure 5.5: From the top, output form NaI(Tl), output form YAP, output from 32 strips from ToT converted to total deposited energy per frame

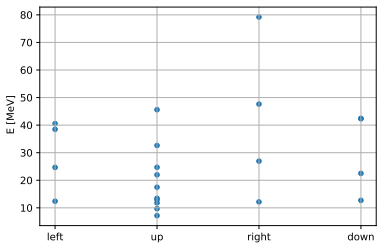

(a) : Strip detector 12 mm from plasma edge

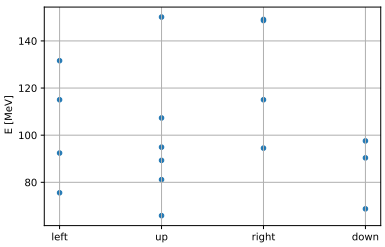

(b) : Strip detector 6 mm from plasma edge

Figure 5.6: Dependence of total deposited energy (averaged to one strip) on sensor orientation.

Conclusion

During plasma discharge in a tokamak, runaway electrons (RE) may emerge. They have a detrimental effect on the vacuum vessel and associated instrumentation. Development in fusion physics is focused on demonstrating the feasibility of thermonuclear fusion in ITER and DEMO. Runaway electrons are considered to be one of a threat to their operation; hence new mitigation strategies and detection methods are being developed.

Silicon semiconductor detectors are widely used in high energy physics as particle tracking detectors. A Silicon detector in a vacuum vessel could provide information about RE's time and position when they lose confinement. SiPMs are considered as a replacement for PMTs in PET tomography since they provide high gain and fast response, and they are not affected by the magnetic field. LYSO crystal, coupled with SiPM, can provide better information of the HXR spectrum, emerging from RE.

Measurements conducted with the silicon strip detector will be used for the development of better shielding. Poor behavior of the SiPM output signal is probably connected to impedance matching. This problem will be further investigated.

Bibliography

[1] J. Wesson and D. J. Campbell, *Tokamaks*, 3rd ed. New York: Oxford University Press, 2004, ISBN: 0-19-850922-7.

[2] P. Kulhánek, *Úvod do teorie plazmatu*, Vyd. 1. Praha: AGA, 2011, ISBN: 978-80-904582-2-2.

[3] `https://www.euro-fusion.org/fileadmin/user_upload/Archive/wp-content/uploads/2011/09/JG05.537-1c.jpg`, Accessed: 2020-09-01.

[4] *Tokamak golem wiki*. [Online]. Available: `http://golem.fjfi.cvut.cz/wiki/` (visited on 07/07/2019).

[5] H. Dreicer, "Electron and Ion Runaway in a Fully Ionized Gas. I", *Physical Review*, vol. 115, no. 2, pp. 238–249, Jul. 1959, ISSN: 0031-899X. DOI: `10.1103/PhysRev.115.238`. [Online]. Available: `https://doi.org/10.1103/physrev.115.238`.

[6] M. Vlainic, "Studies of runaway electrons in compass", eng, PhD thesis, Ghent University, 2017. [Online]. Available: `http://dx.doi.org/10.13140/RG.2.2.27196.13449`.

[7] O. Ficker, "Generation, Losses and Detection of Runaway electrons in tokamaks", 2015. [Online]. Available: `https://physics.fjfi.cvut.cz/publications/FTTF/DP%7B%5C_%7DOndrej%7B%5C_%7DFicker.pdf`.

[8] J. W. Connor and R. J. Hastie, "Relativistic Limitations on Runaway Electrons", *Nuclear Fusion*, vol. 15, no. 3, pp. 415–423, 1975, ISSN: 17414326. DOI: `10.1088/0029-5515/15/3/007`. [Online]. Available: `https://doi.org/10.1088/0029-5515/15/3/007`.

[9] R. S. Granetz, B. Esposito, *et al.*, *An ITPA joint experiment to study runaway electron generation and suppression*, 2014. DOI: `10.1063/1.4886802`. [Online]. Available: `https://doi.org/10.1063/1.4886802`.

[10] H. M. Smith and E. Verwichte, "Hot tail runaway electron generation in tokamak disruptions", *Physics of Plasmas*, vol. 15, no. 7, 2008, ISSN: 1070664X. DOI: `10.1063/1.2949692`.

[11] S. Putvinski, P. Barabaschi, *et al.*, "Halo current, runaway electrons and disruption mitigation in ITER", *Plasma Physics and Controlled Fusion*, 1997, ISSN: 07413335. DOI: 10.1088/0741-3335/39/12B/013.

[12] Y. Gribov, D. Humphreys, *et al.*, "Chapter 8: Plasma operation and control", *Nuclear Fusion*, vol. 47, no. 6, S385–S403, 2007, ISSN: 00295515. DOI: 10.1088/0029-5515/47/6/S08. [Online]. Available: https://doi.org/10.1088/0029-5515/47/6/s08.

[13] A. Rechester and M. Rosenbluth, "Electron heat transport in a tokamak with destroyed magnetic surfaces", *Physical Review Letters*, vol. 40, no. 1, p. 38, 1978.

[14] M. Bakhtiari, G. J. Kramer, and D. G. Whyte, "Momentum-space study of the effect of bremsstrahlung radiation on the energy of runaway electrons in tokamaks", *Physics of plasmas*, vol. 12, no. 10, p. 102 503, 2005.

[15] J. Yu, E. Hollmann, *et al.*, "Visible imaging and spectroscopy of disruption runaway electrons in diii-d", *Physics of Plasmas*, vol. 20, no. 4, p. 042 113, 2013.

[16] G. F. Knoll, *Radiation detection and measurement*, 3rd ed. New York: Wiley, 2000, ISBN: 0471073385.

[17] R. J. E. Jaspers, *Relativistic runaway electrons in tokamak plasmas*. 1995, p. 173, ISBN: 9038604742.

[18] D. Marocco, B. Esposito, *et al.*, "First results on runaway electron studies using the ftu neutron camera", *Fusion Engineering and Design*, vol. 96, pp. 852–855, 2015.

[19] M. Sadowski, L. Jakubowski, and A. Szydlowski, "Adaptation of selected diagnostic techniques to magnetic confinement fusion experiments", *Czechoslovak Journal of Physics*, vol. 54, no. 3, p. C74, 2004.

[20] S. M. Sze and M. K. Lee, *Semiconductor devices, physics and technology*, 3rd ed. Hoboken, N.J.: Wiley, 2012, ISBN: 978-0470-53794-7.

[21] G. Lutz, *Semiconductor radiation detectors : device physics*. Berlin New York: Springer, 2007, ISBN: 978-3-540-71678-5.

[22] Z. Janoska, M. Carna, *et al.*, "Measurement of ionizing particles by the PH32 chip", in *2015 IEEE Nuclear Science Symposium and Medical Imaging Conference, NSS/MIC 2015*, IEEE, 2016, ISBN: 9781467398626. DOI: 10.1109/NSSMIC.2015.7581968. [Online]. Available: https://doi.org/10.1109/nssmic.2015.7581968.

[23] Z. Janoska, T. Benka, *et al.*, "Time of flight measurements with the PH32 chip", *Journal of Instrumentation*, vol. 14, no. 04, pp. C04004–C04004, 2019. DOI: 10.1088/1748-0221/14/04/c04004. [Online]. Available: https://doi.org/10.1088/1748-0221/14/04/c04004.

[24] *Lyso scintillation material*, Saint-Gobain Crystals, 2018. [Online]. Available: https://www.crystals.saint-gobain.com/sites/imdf.crystals.com/files/documents/lyso-material-data-sheet.pdf.

[25] *Lanthanum bromide and enhanced lanthanum bromide*, Saint-Gobain Crystals, 2018. [Online]. Available: https://www.crystals.saint-gobain.com/sites/imdf.crystals.com/files/documents/lanthanum-material-data-sheet.pdf.

[26] Qwerty123uiop, *Photomultiplier tube and scintillator*, Accessed 2020-09-01. [Online]. Available: https://commons.wikimedia.org/wiki/File:PhotoMultiplierTubeAndScintillator.svg.

[27] C. Grupen and B. Shwartz, *Particle Detectors*, 2nd ed., ser. Cambridge Monographs on Particle Physics, Nuclear Physics and Cosmology. Cambridge University Press, 2008. DOI: 10.1017/CBO9780511534966.

[28] *Sipm working principle - ketek gmbh*, Accessed 2020-09-01. [Online]. Available: https://4b0vz81vun5u2kaw7x3w6ptl-wpengine.netdna-ssl.com/wp-content/uploads/2017/01/ketek-sipm-technology-working-principle.png.

[29] *Product data sheet sipm – silicon photomultiplier pm3315-wb-b0*, KETEK GmbH, 2019. [Online]. Available: https://www.ketek.net/wp-content/uploads/2018/12/KETEK-PM3315-WB-B0-Datasheet.pdf.